Vortex structures of rotating spin-orbit-coupled Bose-Einstein condensates

Xiang-Fa Zhou,[1,2] Jing Zhou,[2] and Congjun Wu[1]

[1]*Department of Physics, University of California, San Diego, California 92093, USA*

[2]*Key Laboratory of Quantum Information, University of Science and Technology of China, CAS, Hefei, Anhui 230026, People's Republic of China*

(Received 30 August 2011; revised manuscript received 28 October 2011; published 19 December 2011)

We consider the quasi-two-dimensional two-component Bose-Einstein condensates with Rashba spin-orbit (SO) coupling in a rotating trap. The rotation angular velocity couples to the mechanical angular momentum, which contains a noncanonical part arising from SO coupling. The effects of an external Zeeman term favoring spin polarization along the radial direction is also considered, which has the same form as the noncanonical part of the mechanical angular momentum. The rotating condensate exhibits a variety of rich structures by varying the strengths of the trapping potential and interaction. With a strong trapping potential, the condensate exhibits a half-quantum vortex-lattice configuration. Such a configuration is driven to the normal one by introducing the external radial Zeeman field. In the case of a weak trap potential, the condensate exhibits a multidomain pattern of plane-wave states under the external radial Zeeman field.

DOI: 10.1103/PhysRevA.84.063624 PACS number(s): 03.75.Lm, 05.30.Jp, 67.85.Fg, 03.75.Mn

I. INTRODUCTION

Spin-orbit (SO) coupling plays an important role in various aspects in condensed-matter systems, including spintronics [1] and topological insulators [2,3]. However, SO effects in bosonic systems have not attracted much attention until recently. For example, ^{4}He atoms are spinless and ultracold bosons with nonzero spin are too heavy to exhibit relativistic SO coupling. This situation is significantly changed by the recent experimental progress in both semiconductor exciton systems and cold-atom systems with synthetic gauge fields. Excitons are composite bosons of electrons and holes. Their effective masses are light enough to exhibit relativistic SO coupling. Exotic SO-coupled condensates with stripe- and Skyrmion-type spin texture configurations were theoretically predicted by Wu and Mondragon-Shem [4]. Excitingly, spin textures have been observed in the SO coupled exciton condensates by High *et al.* [5]. On the other hand, many theoretical schemes have been proposed in ultracold atomic systems to create artificial non-Abelian gauge fields by using laser-atom interactions [6–17], which generate effective SO coupling without special relativity.

It has been shown that bosons with SO coupling support exotic ground states beyond the "no-node" theorem [18–21]. This theorem states that the ground-state wave functions of bosons under very general conditions are positive definite, which is essentially a direct result of the Perron-Frobenius theorem of matrix analysis [22]. However, the linear coupling to momentum in the SO coupling invalidates the proof of the no-node theorem. For example, spontaneous time-reversal symmetry-breaking states exhibiting spin-density wave ordering [4,19,23–26] and spontaneous half-quantum vortex configuration [4,19] have been studied. Both of them exhibit either nodal or complex-valued condensate wave functions, and thus are beyond the no-node theorem. Especially, the realization of SO-coupled Bose-Einstein condensates (BEC) of ^{87}Rb [27,28] provides a valuable opportunity to investigate this type of exotic physics, experimentally. Another way to bypass no-node theorem is to employ the metastable excited states, in which no-node theorem does not apply either. For example, cold alkali-metal bosons have been pumped into the high orbitals in optical lattices [29,30]. It was shown that interactions among p-orbital bosons obey an "orbital Hund's rule," which generates a class of orbital superfluid states with complex-valued wave functions breaking time-reversal (TR) symmetry spontaneously [31–36].

On the other hand, vortex properties in rotating BECs are a characteristic topological feature of superfluidity, including ^{4}He and ultracold bosons, which have been studied extensively both experimentally and theoretically [37]. For spinor BECs and Cooper pairing superfluidity with nonzero spin (e.g., superfluid ^{3}He A and B phases), exotic spin textures and fractional quantized vortices can form under rotation [38]. However, to our knowledge, the vortex properties of rotation SO-coupled BECs have not been thoroughly investigated before.

In this paper, we investigate the rotating SO-coupled condensate in a quasi-two-dimensional (2D) harmonic trap with the angular velocity along the z axis. The angular velocity couples to the mechanical angular momentum, whose noncanonical part behaves like a Zeeman term polarizing spin in the radial direction. We also consider the effect from an external Zeeman term with the same form. The single-particle ground states in the absence of interaction can have nonzero vortex numbers, which differ by one in the spin-up and -down components as a result of SO coupling. With many-body interactions, the rotating condensate exhibits a variety of configurations depending on the strengths of the trapping potential and interaction. If the trapping potential is strong and interaction is relatively weak, a half-quantum vortex lattice is formed under rotation. Its spin configuration is a lattice of Skyrmions. The condensate of the spin-up component breaks into disconnected density peaks, which overlap the vortex cores of the spin-down condensate. The presence of the external Zeeman field drives the system from a half-quantum vortex-lattice state to a normal quantum vortex-lattice state. In the case of a weak trap potential, the condensate favors a plane-wave state or a two-plane-wave state with twist phase profiles under rotation. With the external Zeeman

field, the condensate develops a multidomain configuration of plane-wave states. The configuration of wave vectors can be clockwise or counterclockwise depending on the direction of the field.

The rest part of the paper is organized as follows. The model Hamiltonian of the rotating Rashba coupled BEC is introduced in Sec. II. The solution of the single-particle wave function is presented in Sec. III. The rich structures of the vortex configurations with spin textures are given in Sec. IV. Conclusions are given in Sec. V.

II. MODEL HAMILTONIAN

We consider the quasi-2D two-component BECs with Rashba SO coupling in the xy plane subject to a rotation angular velocity Ω_z along the z direction. The free part of the Hamiltonian of Rashba SO coupling under rotation is defined through the standard minimal coupling as

$$H_0 = \int d^3\vec{r}\,\psi_\mu^\dagger(\vec{r})\Big[\frac{1}{2M}(-i\hbar\vec{\nabla} + M\lambda\hat{z}\times\vec{\sigma} - \vec{A})^2 - \mu + V_{\rm ext}(\vec{r}) - \frac{1}{2}M\Omega_z^2(x^2+y^2)\Big]_{\mu\nu}\psi_\nu(\vec{r}), \quad (1)$$

where $\vec{\sigma} = \sigma_x\hat{x} + \sigma_y\hat{y} + \sigma_z\hat{z}$ with $\sigma_{x,y,z}$ the usual Pauli matrices; λ is the Rashba SO coupling strength with the unit of velocity; μ,ν take values of $\uparrow,\downarrow$ as pseudospin indices; $\vec{A} = (-M\Omega_z y, M\Omega_z x, 0)$ is the vector potential from the Coriolis force; $V_{\rm ext}(\vec{r}) = \frac{1}{2}M\omega_T(x^2+y^2)$ is the external harmonic trapping potential; the last term in Eq. (1) is the centrifugal force. The interaction part $H_{\rm int}$ is defined as

$$H_{\rm int} = \frac{g_{\mu\nu}}{2}\int d^3\vec{r}\,\psi_\mu^\dagger(\vec{r})\psi_\nu^\dagger(\vec{r})\psi_\nu(\vec{r})\psi_\mu(\vec{r}). \quad (2)$$

We assume the equal intracomponent interactions as $g_{\uparrow\uparrow} = g_{\downarrow\downarrow} = g$, and intercomponent interaction $g_{\uparrow\downarrow} = gc$ with c a constant coefficient.

Due to the presence of SO coupling, Ω_z couples to the mechanical angular momentum $L^{\rm mech}$, rather than the canonical one L_z. We extract this coupling from Eq. (1) as

$$H_{\rm rot} = -\Omega_z\int d^3\vec{r}\,\psi_\mu^\dagger(\vec{r})[L^{\rm mech}]_{\mu\nu}\psi_\nu(\vec{r}), \quad (3)$$

where

$$L^{\rm mech} = L_z + M\lambda(x\sigma_x + y\sigma_y). \quad (4)$$

Therefore, rotation in the presence of SO coupling induces an effective magnetic-field distribution $\vec{B}_R(\vec{r}) = \Omega_z M\lambda(x,y,0)$ in the xy plane. As we will see below, this noncanonical part in $L^{\rm mech}$ plays a crucial role during the understanding of the single-particle ground-state properties.

For later convenience, we also introduce an external spatially dependent Zeeman term as

$$H_B = -\int d^3r\,\psi_\mu^\dagger(\vec{r})(B_{{\rm ex},x}\sigma_x + B_{{\rm ex},y}\sigma_y)_{\mu\nu}\psi_\nu(\vec{r}), \quad (5)$$

where $\vec{B}_{\rm ex}(\vec{r}) = (B_0 x, B_0 y, 0)$ varies linearly in the xy plane. Such a term can tune the strength of the noncanonical part of the mechanical momentum, which renders the model adjustable in a wider range of the parameter space.

Many efforts have been made to implement the above Hamiltonian in ultracold atomic gases. Several schemes have been proposed to generate Rashba SO coupling [6,16,17] with tunable SO-coupling strength. In particular, proposals in Refs. [16,17] have the advantage to overcome the drawback of the spontaneous emission in the tripod scheme. The spatially dependent Zeeman term H_B can be generated through coupling two spin components using two standing waves in the x and y directions with a phase difference of $\pi/2$. The resulting Rabi coupling is written as

$$-\Omega[\sin(k_L x) + i\,\sin(k_L y)]\psi_\downarrow^\dagger(\vec{r})\psi_\uparrow(\vec{r}) + \text{H.c.} \quad (6)$$

In the region of $x,y \ll 2\pi/k_L$, it reduces to the desired form of Eq. (5) with $B_0 = \Omega k_L$.

III. SINGLE-PARTICLE SPECTRA

We start with the noninteracting Hamiltonian $H_0 + H_B$ to gain some intuition. The confining trap is characterized by the length scale $l = \sqrt{\hbar/M\omega}$. We define another length scale $l_{\rm so} = \hbar/(M\lambda)$ from SO coupling. The ratio between them, $\alpha = l/l_{\rm so}$, is a dimensionless parameter to describe the strength of SO coupling. For the typical setup used in the NIST group [28], $\alpha \sim 10$. Below, we vary the values of α from 0 to 10. Experimentally, the regime of small α can be reached by using a deeper trap potential.

Without the confining potential and rotation, the single-particle eigenstates are of the form

$$\psi_{\pm,\vec{k}} = e^{i\vec{k}\cdot\vec{r}}|\pm,\vec{k}\rangle, \quad (7)$$

where $|\pm,\vec{k}\rangle = \frac{1}{\sqrt{2}}(1, \mp e^{i\theta_{\vec{k}}})^T$ and $\theta_{\vec{k}}$ is the azimuthal angle of $\vec{k}$. Since the condensate is uniform along the $\hat{z}$ direction, we always have $k_z = 0$ for the ground state. The corresponding dispersion relations come into two branches $\epsilon_\pm = \hbar^2(k^2 \pm 2k_0 k)/(2M)$, with $k_0 = 1/l_{\rm so}$. Therefore, the single-particle ground states are infinitely degenerate along a ring in momentum space with radius k_0.

The external harmonic potential has the important effect of lifting the degeneracy along the Rashba ring, as pointed out in Ref. [4]. In the momentum representation, the harmonic potential becomes $\frac{1}{2}M\omega^2(i\hbar\vec{\nabla}_{\vec{k}} - \vec{A}')^2$ in the lower branch and couples different plane-wave states around the Rashba ring, where $\vec{A}'(\vec{k}) = i\langle\psi_{-,\vec{k}}|\vec{\nabla}_{\vec{k}}|\psi_{-,\vec{k}}\rangle$ corresponding to a π flux at the origin. Therefore, the motion along the Rashba ring is quantized and maintains time-reversal (TR) invariance. The single-particle spectra exhibit the fermion-type Kramer degeneracy with $T^2 = -1$. The lowest single-particle eigenstates carry $j_z = \pm\frac{1}{2}$. As shown in Ref. [4], the angular quantization gives rise to the dispersion on j_z as

$$\frac{1}{\alpha^2}|j_z|^2\hbar\omega_T. \quad (8)$$

On the other hand, the radial quantization is the same as in the ordinary harmonic trap, which is at the order of $\hbar\omega_T$ [4]. In the strong SO-coupling limit, i.e., $\alpha \gg 1$, the dispersion over j_z is nearly flat. Thus the radial quantum number can be viewed as a band index, and the quantum number j_z marks each state in the band.

To be more precise, we define two independent annihilation operators as $\hat{a}_d = \frac{1}{2}(\bar{z} + 2\partial_z)$ and $\hat{a}_g = \frac{1}{2}(z + 2\partial_{\bar{z}})$, where $z = (x \pm iy)/l$ and $\bar{z}$ is the complex conjugate of z [37,39]. The single-particle Hamiltonian can be rewritten in the unit $\hbar\omega$ as

$$H_0 + H_B = (1-\rho)\hat{N}_d + (1+\rho)\hat{N}_g + 1 + \alpha\{[(1-\kappa)\hat{a}_d - (1+\kappa)\hat{a}_g^\dagger]\sigma^+ + \text{H.c.}\}, \quad (9)$$

where

$$\rho = \Omega_z/\omega, \quad \hat{N}_d = \hat{a}_d^\dagger\hat{a}_d, \quad \hat{N}_g = \hat{a}_g^\dagger\hat{a}_g, \quad \sigma^+ = \tfrac{1}{2}(\sigma_x + i\sigma_y), \quad (10)$$

and $\kappa = \gamma + \rho$ with $\gamma = B_0/(M\omega\lambda)$. The corresponding canonical angular momentum reads $L_z = \hbar l_z = \hbar(\hat{N}_d - \hat{N}_g)$. The κ term represents the combined effect from the noncanonical part of H_{rot} and the Zeeman term H_B.

We diagonalize Eq. (9) to obtain the single-particle spectra, and present the solutions in the coordinate representation, in which the ground-state wave function reads as

$$e^{im\phi}\begin{pmatrix} f(r) \\ g(r)e^{i\phi}\end{pmatrix}. \quad (11)$$

The total canonical angular momentum $j_z = l_z + \frac{1}{2}\sigma_z = m + \frac{1}{2}$ remains a conserved quantity; thus the canonical orbital angular momenta in the two spin components differ by one due to SO coupling. Figure 1 shows m as a function of the rotational angular velocity ρ for different external magnetic field $\vec{B}_{\text{ex}}$ at $\alpha = 4$. In the absence of $\vec{B}_{\text{ex}}$, the total angular momentum $j_z = -\frac{1}{2}$ for small ρ and decreases when $\rho \to 1$. Introducing the field $\vec{B}_{\text{ex}}$ changes the ground state dramatically. If $\vec{B}_{\text{ex}}$ is parallel to the induced magnetic field $\vec{B}_R$, i.e., $\gamma > 0$, j_z first decreases then increases with the rotational angular velocity ρ. However, for $\gamma < 0$, j_z increases with ρ monotonically.

The above results can be understood as follows. In the case of $\Omega_z = 0$, the two states $\phi_{j_z=\pm\frac{1}{2}}$ are degenerated due to TR symmetry. Since only one of the two spin components carries a vortex, the ground state can be viewed as a half-quantum vortex state with the density profiles of two spin components shown in Fig. 2. The spin-density distributions exhibit Skyrmion-type

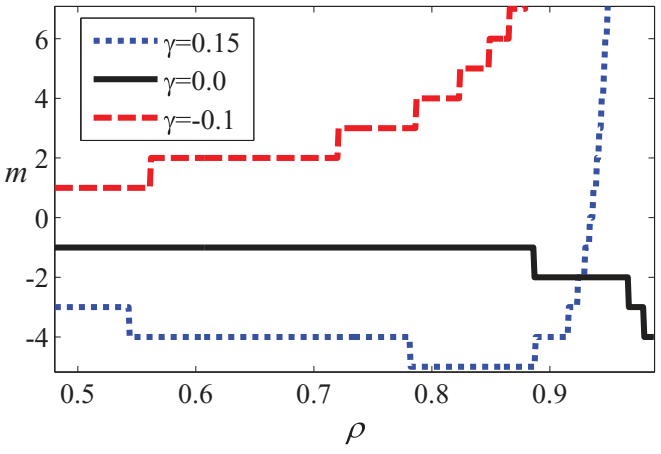

FIG. 1. (Color online) Canonical angular momenta m of the single-particle ground states described in Eq. (11) vs ρ for $\gamma = -0.1$, 0.0, and 0.15, respectively.

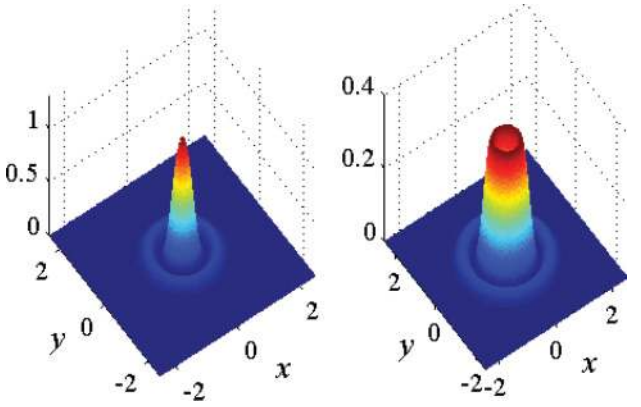

FIG. 2. (Color online) Density profiles of spin-up and -down components for the single-particle ground state $\phi_{j_z=\frac{1}{2}}$ with the parameter values of $\alpha = 4$ and $\rho = \gamma = 0$. Only the spin-down component carries a vortex. The corresponding density profile for $\phi_{j_z=-\frac{1}{2}}$ is obtained by interchanging the spin indices. Here we use the length unit defined by the harmonic trap.

texture configurations, as depicted in Figs. 3(a) and 3(b). Intuitively, one might expect that an infinitesimal Ω_z selects the $\phi_{j_z=\frac{1}{2}}$ state, since it has lower rotational energy $-\Omega_z\langle L_z\rangle$. However, the presence of the induced magnetic field $\vec{B}_R$ contributes another term to the total rotational energy of the system as

$$\langle H_{\text{rot}}\rangle = -\Omega_z\langle L_z\rangle - \vec{B}_R\cdot\langle\vec{\sigma}\rangle. \quad (12)$$

The spin pattern $\langle\vec{\sigma}\rangle$ for $\phi_{j_z=\frac{1}{2}}$ in the xy plane is antiparallel to $\vec{B}_R$ near the trap center [see Fig. 3(a)], which is energetically unfavorable. Therefore, when $-\vec{B}_R\cdot\langle\vec{\sigma}\rangle$ dominates, j_z of the ground state can be $-\frac{1}{2}$ for a rotating trap. As Ω_z increases, the condensates expand, which also favors the magnetic energy

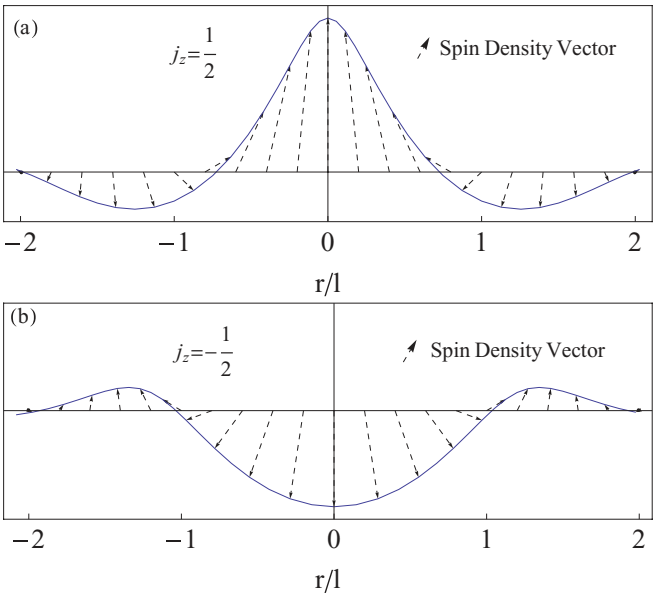

FIG. 3. (Color online) Spin-density vector distributions along the x axis lie in the xz plane as shown in (a) $j_z = \frac{1}{2}$ and (b) $j_z = -\frac{1}{2}$ with $\alpha = 4$ and $\rho = \gamma = 0$. They are time-reversal counterparts to each other, and both exhibit the Skyrmion-type texture configuration.

term. The total angular momentum j_z can decrease even when ρ increases. Such a counterintuitive effect for the ground state constitutes a characteristic feature of SO-coupled BECs in a rotating trap. Introducing the external magnetic field $\vec{B}_{\rm ex}$ strengthens or weakens the effect induced by $\vec{B}_R$ depending on its direction, which explains the different behaviors of m with ρ for $\gamma > 0$ and $\gamma < 0$, as shown in Fig. 1.

IV. VORTEX CONFIGURATIONS OF ROTATING SO-COUPLED BEC

Interaction effects in the absence of rotation have been investigated extensively in the literature, and are summarized below. In the case of a strong trapping potential and weak interaction, the single-particle energy dominates. The condensate maintains rotational symmetry but spontaneously breaks TR symmetry [4,19]. One spin component carries one vortex and the other is nonrotating; thus the condensate possesses a half-quantum vortex. The total angular momentum of each particle is $|j_z| = \frac{1}{2}$. In momentum space, this kind of ground state distributes uniformly around the Rashba ring. On the contrary, if the trapping potential is weak and interaction is strong, the condensate breaks rotational symmetry. The condensate is approximately the superposition of plane-wave states modified by the cylindrical boundary condition. Results based on the Gross-Pitaevskii (GP) equation show that the spin-spiral condensate with two counterpropagating plane waves is favored at $c > 1$, while a single plane wave is favored at $c < 1$ [23–26]. These two different condensates are degenerate for the spin-independent interactions, i.e., $c = 1$. However, calculations including quantum fluctuations of the zero-point energy show that the spin-spiral state wins at $c = 1$, and thus shifts the phase boundary to a smaller value of c [19].

In this section, we study the vortex configurations of SO-coupled BECs in both cases. The results of strong trapping potentials and weak interactions are presented in Sec. IV A, and those of the opposite limit are presented in Sec. IV B.

A. Vortex-lattice configurations with a strong trapping potential

In this subsection, we turn on rotation and consider a strong trapping potential with a small value of α. The ground-state condensate is obtained by numerically solving the following SO-coupled GP equation. We assume that the condensate is uniform along the z axis, and define the normalized condensate wave function $(\tilde{\psi}_\uparrow, \tilde{\psi}_\downarrow)^T$ satisfying $\int d^2\vec{r}(|\psi_\uparrow|^2 + |\psi_\downarrow|^2) = 1$. The dimensionless version of the GP equation can then be written as

$$\frac{\mu}{\hbar\omega}\tilde{\psi}_\uparrow = \hat{T}_{\uparrow v}\tilde{\psi}_v + \beta(|\tilde{\psi}_\uparrow|^2 + c|\tilde{\psi}_\downarrow|^2)\tilde{\psi}_\uparrow, \tag{13a}$$

$$\frac{\mu}{\hbar\omega}\tilde{\psi}_\downarrow = \hat{T}_{\downarrow v}\tilde{\psi}_v + \beta(|\tilde{\psi}_\downarrow|^2 + c|\tilde{\psi}_\uparrow|^2)\tilde{\psi}_\downarrow, \tag{13b}$$

where

$$\hat{T} = -\frac{1}{2}l^2\left(\partial_x^2 + \partial_y^2\right) + \alpha l(-i\partial_y\sigma_x + i\partial_x\sigma_y) + \frac{1}{2l^2}(x^2 + y^2) - \rho(-ix\partial_y + iy\partial_x) - \frac{\alpha\kappa}{l}(x\sigma_x + y\sigma_y), \tag{14}$$

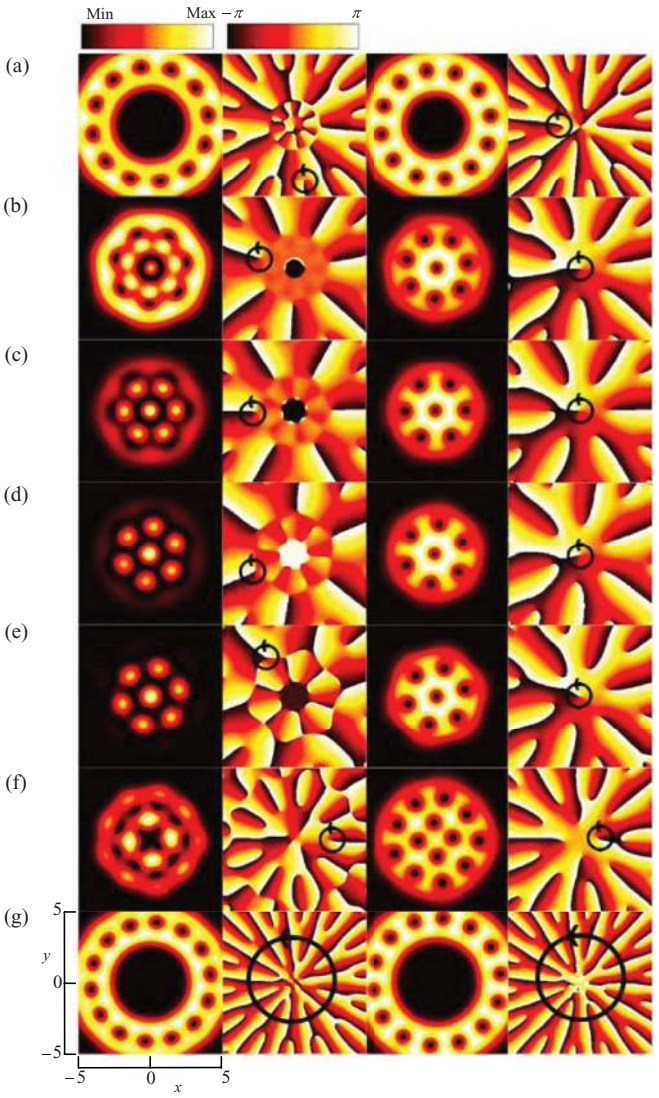

FIG. 4. (Color online) From left to right: the density and phase profiles of spin-up and -down components with parameter values of $\alpha = 0.5$, $\beta = 10$, $\rho = 0.97$, and $c = 1$. From (a) to (g), γ is taken as 0.5, 0.25, 0.1, 0.0, −0.1, −0.25, and −0.5, respectively. At small values of $|\gamma|$ in (c)–(e), a half-quantum vortex lattice is formed near the trap center. The spin-up component breaks into several density peaks, and the low-density region is connected. By increasing the magnitude of $|\gamma|$ [(b) and (f)], the half-quantum vortex lattice evolves to the normal vortex lattice. For the large value of $|\gamma| = 0.5$ [(a) and (g)], the condensates show a lattice configuration around a ring. The black circle with an arrow indicates the direction of the circulation around the vortex core. The unit of length for the figures is l.

where μ is the chemical potential; the interaction parameter $\beta = gN/(\hbar\omega l_z)$; N is the particle number in the condensate; l_z is the system size along the z direction.

The density and phase configurations at various parameters are shown in Figs. 4(a)–4(g), which exhibit rich structures of vortex lattice. We look at Fig. 7(d) in the absence of $\vec{B}_{\rm ex}$, i.e., $\gamma = 0$. The density distribution of the spin-up component is composed of several disconnected density peaks near the trap center. On the other hand, the low-density region is connected in contrast to the usual vortex-lattice structure, in

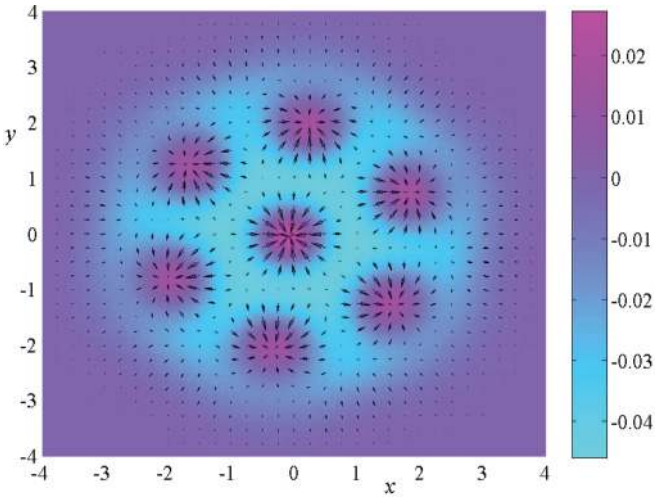

FIG. 5. (Color online) Ground-state spin-density vector of Fig. 7(d) with parameter values of $\alpha = 0.5$, $\beta = 10$, $\rho = 0.97$, $c = 1$, and $\gamma = 0$. The projection of $\langle\vec{\sigma}\rangle$ in the xy plane is shown as black vectors. A color map is used to illustrate the $\langle\sigma_z\rangle$ component. The unit of length for the figure is l.

which the low-density region of vortex cores is disconnected. Nevertheless, we identify the locations of the singular points of the phase distribution pattern around which the phase winds with an integer number. These singular points are squeezed out to the edge of the condensate. On the other hand, the spin-down component exhibits the regular vortex-lattice structure, whose vortex cores overlap with the density peaks of the spin-up component. Around each vortex core, the two spin components show a half-quantum vortex configuration as those depicted in Fig. 2. Therefore, the condensates of two components together exhibit a lattice of half-quantum vortices. The corresponding spin-density vector $\langle\vec{\sigma}\rangle$ shows a Skyrmion-lattice structure, as shown in Fig. 5.

Now we turn on the external Zeeman term, Eq. (5). For both cases of $\gamma > 0$ and $\gamma < 0$, at small values of $|\gamma|$, the half-quantum vortex lattice still forms, which is similar to that at $\gamma = 0$ as depicted in Figs. 4(b), 4(c), and 4(e). As we increase the strength of $\vec{B}_{\rm ex}$, i.e., $|\gamma|$, more vortices appear, as depicted in Figs. 4(b) and 4(f). The condensates of the spin-up component gradually evolve to the usual vortex-lattice configuration. The high-density region becomes connected, while the density minima become disconnected vortex cores. On the other hand, the condensates of the spin-down component remain the usual vortex-lattice configuration. For even larger values of $|\gamma|$, the ring-shaped vortex lattice with a giant vortex core is observed as shown in Figs. 4(a) and 4(g). This is because the combined effect of the harmonic trap $V_{\rm ext}(\vec{r})$ and the additional Zeeman term H_B shifts the potential minimum to a ring in real space with the radius of $r = \alpha\gamma l = |B_0|/(M\omega^2)$. The condensates of both spin-up and -down components distribute around this ring and from a giant vortex configuration. Additionally, the Zeeman term grows linearly as r increases and favors in-plane polarization of $\vec{S}$. As a result, the vortex cores of the spin-up and -down components overlap with each other.

We stress that, in all cases in Figs. 4(a)–4(g), the vortex numbers in the spin-up and -down components differ by one, which is a characteristic feature brought by SO coupling. As shown in Eq. (11), for the eigenstate of the single-particle Hamiltonian with $j_z = m + \frac{1}{2}$, the two spin components carry different canonical orbital angular momenta m and $m + 1$, respectively. In the presence of interaction, the giant vortex splits into a lattice of single-quantum vortices in each spin component. Nevertheless, the total vortex number in each component remains unchanged and differs by one.

B. Weak trapping potential

In this subsection, we study the rotating SO-coupled BEC with a weak trapping potential and strong interactions.

Figure 6 shows the density and phase profiles of each spin component in the absence of external magnetic field $\vec{B}$, i.e., $\gamma = 0$. In Fig. 6(a) with $c < 1$, the condensate is a twisted plane-wave state subject to the cylindrical boundary condition. The spin polarization mainly lies in the xy plane. In the representation eigenbasis of s_z, the spin-up and -down components show nearly the same distributions of density and phase profiles. Nevertheless, the phase distribution is distorted from the exact plane-wave state. On the other hand, as depicted in Fig. 6(b), at $c > 1$ the spin-spiral-like condensate with two counterpropagating plane waves is still favored with twisted phase profiles. As shown in Fig. 6(c), increasing the angular velocity ρ gives rise to an intermediate configuration between the distorted spin-spiral and the single-plane wave states. In all the patterns, vortices locate either on the edge of the condensate or the density minima of each component.

Next, we consider the case of $\gamma \neq 0$. Introducing H_B significantly enriches the structures of the rotating SO-coupled condensates. We only consider a small angular velocity at $\rho = 0.1$ for the reason of numerical convergence, but vary the

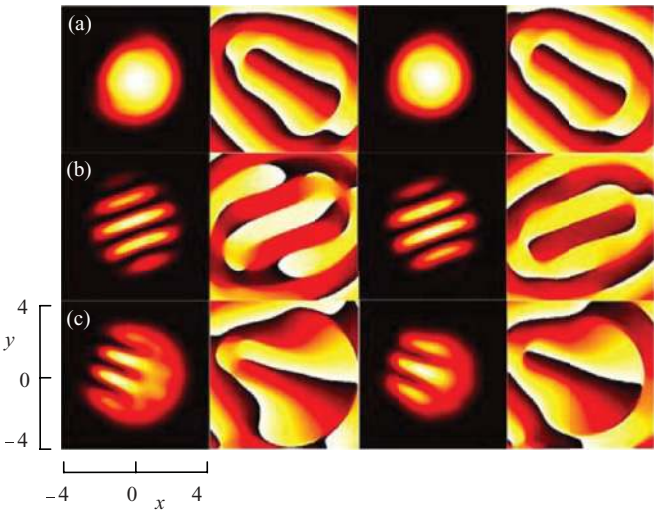

FIG. 6. (Color online) From left to right: the density and phase profiles of spin-up and -down components with the parameter values of $\alpha = 2.5$, $\beta = 40$, and $\gamma = 0$. (a) $c = 0.6$ and $\rho = 0.2$; a plane-wave-like state is obtained with a distorted phase pattern; (b) $c = 1.2$ and $\rho = 0.2$; the spin-spiral condensate is favored; (c) $c = 1.2$ and $\rho = 0.5$; the condensate exhibits an intermediate configuration between those of (a) and (b). The color scales for the density and phase distributions are the same as those in Fig. 4. The unit of length for the figures is l.

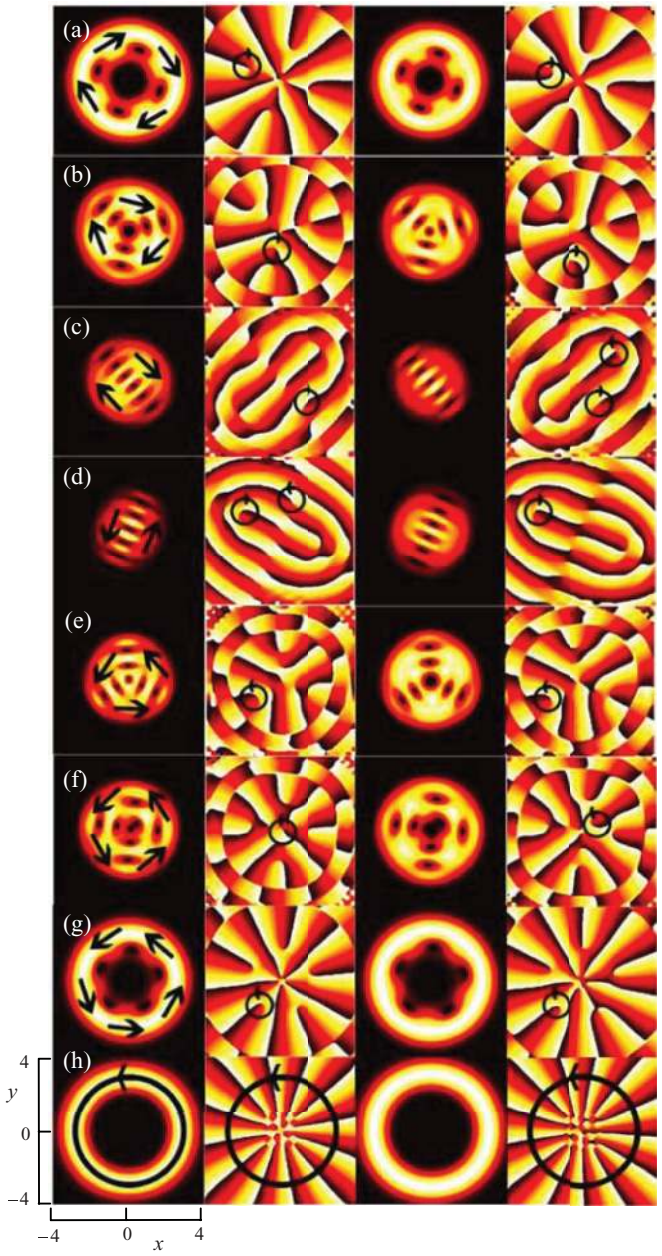

FIG. 7. (Color online) From left to right: the density and phase profiles of spin-up and -down components with parameter values of $\alpha = 4$, $\beta = 20$, $c = 1$, and $\rho = 0.1$. From (a) to (h), γ is taken as $0.5, 0.3, 0.1, -0.05, -0.25, -0.35, -0.6$, and -0.7, respectively. The black arrow in each domain represents the local wave-vector direction of the corresponding plane-wave state, which shows a clockwise or counter-clockwise configuration depending on the sign of γ. For sufficiently large values of $|\gamma|$, condensates distribute around a ring in space forming a giant vortex. The color scales for the density and phase distributions are the same as that in Fig. 4. The black circle with an arrow indicates the direction of the circulation around the vortex core. The unit of length for the figures is l.

values of γ from 0.5 to -0.7, as presented in Figs. 7(a)–7(h), respectively. With small and intermediate values of $|\gamma|$ [e.g., Figs. 7(b)–3(a)], the condensate breaks into several domains. Inside each domain, the condensate can be approximated as a single plane-wave state. Vortices center around the local density minima. The local wave vectors are configured such that the local spin polarization $\langle \vec{S} \rangle$ aligns along the local Zeeman field of $\vec{B}_{\rm ex}(\vec{r})$. If $\gamma > 0$, at which the external Zeeman field enhances the rotation induced ones, we obtain a clockwise configuration of wave vectors. There is one more vortex with the negative phase winding in the spin-up component than in the spin-down component, which reflects the "antiparamagnetic" feature. On the contrary, if $\gamma < 0$, the counterclockwise patterns of wave vectors are favored. Similarly, the spin-down component also carries one more vortex than the spin-up component.

At small values of $|\gamma|$, two domains are formed as depicted in Figs. 7(c) and 3(d). The vortices organize into straight lines between two domains. A variational wave function is constructed as

$$\tilde{\psi}(\vec{r}) \sim \left[f_-(x) e^{-i\frac{\theta}{2}} \psi_{-,-\vec{k}_0} + f_+(x) e^{i\frac{\theta}{2}} \psi_{-,\vec{k}_0} \right] \frac{e^{-r^2/(2a^2)}}{\sqrt{\pi}\sigma}, \tag{15}$$

where, without loss of generality, we choose the wave vector $\vec{k}_0 = k_0 \vec{e}_y$; a is the radius of the condensate; θ is the relative phase difference between the two plane wave domains; $|f_{-,+}(x)|^2 = (e^{\pm x/W} + 1)^{-1}$ are smeared step functions with W the width of the domain wall. We assume $\sigma \gg (W, 1/k_0)$. Such a variational wave function has a negligible contribution to the energy term $\langle H_{\rm rot} \rangle$. This explains why the two-domain pattern is absent by increasing the rotational angular velocity ρ only, but appears immediately even at small values of $|\gamma|$. With increasing $|\gamma|$, the condensate breaks into more and more domains as in Figs. 7(b), 7(e), and 7(f).

As $|\gamma|$ increases further, domains connect together as a giant vortex as shown in Figs. 7(a), 7(g), and 7(h). The condensates of both spin-up and -down components distribute around a ring with the radius of $\alpha|\gamma|l$ and overlap each other. This is a giant vortex configuration with a texture of spin aligned along the radial direction. The phase winding numbers of the spin-up and -down components differ by one due to the SO coupling.

V. CONCLUSION

To summarize, we have considered the vortex structures of SO-coupled BECs in a rotating trap combined with an external spatially dependent Zeeman field. In the case of strong confining potentials and weak interactions, the condensate exhibits vortex-lattice structures. By varying the magnitude of the external Zeeman field, the configuration evolves from a half-quantum vortex lattice to a normal one. In the opposite limit, the condensate develops multidomain patterns with the external Zeeman field. Each domain represents a local plane-wave state, whose wave vector exhibits a clockwise or counterclockwise configuration. Domain boundaries play the role of like vortices.

Note added. Recently, we noticed a recent paper studying the rotating Rashba SO coupled BEC, which considered a special case in the presence of the extra term of Eq. (5) with $\gamma = -\rho$ [40]. Our work has studied the general cases, including the pure rotation without the external fields, which corresponds to $\gamma = 0$. We have also noticed a recent work [41] by Radić *et al.*, where the effective Hamiltonians under different kinds of experimental situations have been discussed.

In that framework, the effective magnetic field $\vec{B}_R$ appears when we rotate the entire experimental setup along the $\hat{z}$ axis.

ACKNOWLEDGMENTS

X.F.Z. gratefully acknowledges the support of NFRP (2011CB921204, 2011CBA00200), NNSF (60921091), NSFC (11004186), CUSF, SRFDP (20103402120031), and the China Postdoctoral Science Foundation. C.W. is supported by NSF-DMR1105945 and AFOSR-YIP program. C.W. acknowledges Aspen Center of Physics, where part of this work was done. C.W. and X.F.Z. thank H. Pu, H. Hu, and X. J. Liu for helpful discussions.

[1] I. Zutic, J. Fabian, and S. Das Sarma, Rev. Mod. Phys. **76**, 323 (2004).
[2] M. Z. Hasan and C. L. Kane, Rev. Mod. Phys. **82**, 3045 (2010).
[3] X. L. Qi and S. C. Zhang, Rev. Mod. Phys. **83**, 1057 (2011).
[4] C. Wu and I. Mondragon-Shem, e-print arXiv:0809.3532.
[5] A. A. High, A. T. Hammack, J. R. Leonard, S. Yang, L. V. Butov, T. Ostatnicky, A. V. Kavokin, and A. C. Gossard, e-print arXiv:1103.0321.
[6] J. Ruseckas, G. Juzeliūnas, P. Öhberg, and M. Fleischhauer, Phys. Rev. Lett. **95**, 010404 (2005).
[7] K. Osterloh, M. Baig, L. Santos, P. Zoller, and M. Lewenstein, Phys. Rev. Lett. **95**, 010403 (2005).
[8] S. L. Zhu, H. Fu, C. J. Wu, S. C. Zhang, and L. M. Duan, Phys. Rev. Lett. **97**, 240401 (2006).
[9] I. I. Satija, D. C. Dakin, and C. W. Clark, Phys. Rev. Lett. **97**, 216401 (2006).
[10] X. J. Liu, X. Liu, L. C. Kwek, and C. H. Oh, Phys. Rev. Lett. **98**, 026602 (2007).
[11] T. D. Stanescu, C. Zhang, and V. Galitski, Phys. Rev. Lett. **99**, 110403 (2007).
[12] G. Juzeliunas, J. Ruseckas, A. Jacob, L. Santos, and P. Ohberg, Phys. Rev. Lett. **100**, 200405 (2008).
[13] J. Y. Vaishnav and C. W. Clark, Phys. Rev. Lett. **100**, 153002 (2008).
[14] I. B. Spielman, Phys. Rev. A **79**, 063613 (2009).
[15] G. Juzeliūnas, J. Ruseckas, and J. Dalibard, Phys. Rev. A **81**, 053403 (2010).
[16] J. D. Sau, R. Sensarma, S. Powell, I. B. Spielman, and S. D. Sarma, Phys. Rev. B **83**, 140510(R) (2011).
[17] D. L. Campbell, G. Juzeliūnas, and I. B. Spielman, Phys. Rev. A **84**, 025602 (2011).
[18] T. D. Stanescu, B. Anderson, and V. Galitski, Phys. Rev. A **78**, 023616 (2008).
[19] C. Wu, I. Mondragon-Shem, and X. F. Zhou, Chin. Phys. Lett. **28**, 097102 (2011).
[20] C. Wu, Mod. Phys. Lett. **23**, 1 (2009).
[21] W. Yao and Q. Niu, Phys. Rev. Lett. **101**, 106401 (2008).
[22] R. B. Bapat and T. Raghavan, *Non-negative Matrices and Applicatons* (Cambridge University Press, Cambridge, UK, 1997).
[23] T.-L. Ho and S. Zhang, Phys. Rev. Lett. **107**, 150403 (2011).
[24] C. Wang, C. Gao, C. M. Jian, and H. Zhai, Phys. Rev. Lett. **105**, 160403 (2010).
[25] S.-K. Yip, Phys. Rev. A **83**, 043616 (2011).
[26] Y. Zhang, L. Mao, and C. Zhang, e-print arXiv:1102.4045 (to appear in Phys. Rev. Lett.).
[27] Y.-J. Lin *et al.*, Nature (London) **462**, 628 (2009).
[28] Y.-J. Lin, K. Jiménez-García, and I. B. Spielman, Nature (London) **471**, 83 (2011).
[29] T. Müller, S. Folling, A. Widera, and I. Bloch, Phys. Rev. Lett. **99**, 200405 (2007).
[30] G. Wirth, M. Olschlager, and A. Hemmerich, Nature Phys. **7**, 147 (2011).
[31] A. Isacsson and S. M. Girvin, Phys. Rev. A **72**, 053604 (2005).
[32] W. V. Liu and C. Wu, Phys. Rev. A **74**, 013607 (2006).
[33] C. Wu, W. V. Liu, J. E. Moore, and S. Das Sarma, Phys. Rev. Lett. **97**, 190406 (2006).
[34] A. B. Kuklov, Phys. Rev. Lett. **97**, 110405 (2006).
[35] V. M. Stojanovic, C. Wu, W. V. Liu, and S. DasSarma, Phys. Rev. Lett. **101**, 125301 (2008).
[36] M. Olschlager, G. Wirth, and A. Hemmerich, Phys. Rev. Lett. **106**, 015302 (2011).
[37] A. L. Fetter, Rev. Mod. Phys. **81**, 647 (2009).
[38] M. M. Salomaa and G. E. Volovik, Rev. Mod. Phys. **59**, 533 (1987); K. Kasamatsu, M. Tsubota, and M. Ueda, Phys. Rev. Lett. **91**, 150406 (2003); E. J. Mueller and T.-L. Ho, *ibid.* **88**, 180403 (2002).
[39] I. Mondragón-Shem, Undergraduate thesis, Instituto de Física Facultad de Ciencias Exactas y Naturales, Universidad de Antioquia, 2010.
[40] X. Q. Xu and J. H. Han, Phys. Rev. Lett. **107**, 200401 (2011).
[41] J. Radić, T. A. Sedrakyan, I. B. Spielman, and V. Galitski, Phys. Rev. A **84**, 063604 (2011).